Green Energy and Resources 4 (2026) 100202

Contents lists available at ScienceDirect

Green Energy and Resources

journal homepage: www.journals.elsevier.com/green-energy-and-resources

Research Article

Mechanistic insights into catalytic co-pyrolysis of cellulose and polyethylene via ReaxFF molecular dynamics simulations

Sijia Li[a], Heping Li[a,*], Jianle He[b,c,*], Muye Feng[d], Zhengcheng Wen[a], Shenghao Wang[a], Dingyi Wang[a], Tianjun Shi[a], Zhongze Bai[e], Kaige Wang[b]

[a] Institute for Energy Studies, Hangzhou Dianzi University, Hangzhou, 310018, China
[b] State Key Laboratory of Clean Energy Utilization, Zhejiang University, Hangzhou, 310027, China
[c] Huadian Electric Power Research Institute Co., Ltd., Hangzhou, 310030, China
[d] School of Mechanical and Power Engineering, Nanjing Tech University, Nanjing, 211816, China
[e] Department of Mechanical Engineering, University College London, London, WC1E 7JE, UK

ARTICLE INFO

Keywords:
Cellulose
Polyethylene
Catalytic co-pyrolysis
Fe_2O_3
ReaxFF-MD

ABSTRACT

The catalytic co-pyrolysis of biomass and plastics is a promising strategy for improving waste conversion and regulating product distribution. In this study, ReaxFF molecular dynamics simulations were used to compare cellulose-polyethylene co-pyrolysis systems with and without Fe_2O_3 nanocluster, aiming to obtain atomistic insights into the role of Fe_2O_3 under accelerated high-temperature simulation conditions. Product analysis showed that in Fe_2O_3 catalytic co-pyrolysis system, the tendency toward the formation of light liquid products became more pronounced within the temperature range of 2200-2600 K, which was associated with the competition between rapid cracking and secondary fragment-growth or recombination processes. Bond-evolution analysis indicated that Fe_2O_3 facilitated the overall decay of C-C and C-H bonds. The apparent activation energies derived from the C-C and C-H bond-count decay model decreased from 100.69 to 86.86 kJ/mol in the non-catalytic system to 88.72 and 77.87 kJ/mol in the catalytic system, respectively. Fe-O bond tracking further suggested temperature-dependent lattice-oxygen loss, oxygen exchange with cellulose-derived oxygen, and the formation of oxygen-deficient Fe sites, which contributed to the enhanced formation of H_2O and CO. Reaction pathway analysis suggested that Fe_2O_3 modified the formation routes of CH_4, C_2H_4, C_2H_2, and CH_2O by promoting oxygen transfer and altering the evolution of oxygen-containing intermediates. These results provide simulation-based mechanistic insights into Fe_2O_3 catalyze cellulose-polyethylene co-pyrolysis and offer hypotheses for future experimental validation.

List of abbreviation

Abbreviation	Definition
CE	cellulose
PE	polyethylene
CP	CE-PE co-pyrolysis
CCP	CE-PE-Fe_2O_3 catalytic co-pyrolysis
ReaxFF-MD	Reactive force field molecular dynamics
C1-C4	gaseous products
C5-C19	light liquid products
C20-C39	heavy liquid products
C40+	char products
Lattice-O	the lattice oxygen of the Fe_2O_3
CE-O	oxygen from cellulose

1. Introduction

The growing concerns over fossil fuel depletion and environmental degradation have rendered the development of sustainable alternative energy sources an urgent necessity. Among various renewable energy conversion technologies, thermochemical conversion of biomass (e.g., pyrolysis, gasification) (Zou et al., 2015; Liu et al., 2025) has emerged as a critical approach to addressing energy and environmental challenges due to its high efficiency and adaptability (Hu et al., 2020; Yuan et al., 2022; Xie et al., 2023). Lignocellulosic biomass, as one of the primary feedstocks, contains cellulose (CE) as its dominant component (~50 wt %), which exhibits substantial potential in sustainable fuel production owing to its carbon-neutral nature and abundant availability. The molecular structure of CE, characterized by β(1,4)-glycosidic bonds,

* Corresponding authors.
E-mail addresses: peacelee@hdu.edu.cn (H. Li), jianle-he@chder.com (J. He).

https://doi.org/10.1016/j.gerr.2026.100202
Received 23 January 2026; Received in revised form 20 May 2026; Accepted 22 May 2026
2949-7205/© 2026 The Authors. Published by Elsevier B.V. on behalf of Shandong University. This is an open access article under the CC BY license (http://creativecommons.org/licenses/by/4.0/).

provides a unique framework for conversion into high-value products (Khatami et al., 2012). Nevertheless, its practical application still faces significant technological bottlenecks.

The core challenge in efficient CE conversion stems from its molecular composition: its inherent high oxygen content (40%-50%) and low hydrogen content (5%-7%) lead to poor-quality bio-oil from standalone pyrolysis, manifesting as excessive oxygen content, low energy density, and poor storage stability, thereby hindering direct use as transportation fuel (Mortensen et al., 2011; Krutof and Hawboldt, 2018; Ahmed et al., 2020; Liu et al., 2025). Although existing upgrading strategies are theoretically feasible, they are generally constrained by process complexity and high energy consumption. Simultaneously, the escalating crisis in plastic waste management demands innovative solutions. According to 2023 statistics, only 10% of the 70 billion tons of global plastic production has been effectively recycled, with the remainder predominantly treated via incineration or landfilling—methods that release persistent organic pollutants and greenhouse gases, posing severe threats to ecosystems (Armenise et al., 2021; Muhammad and Manos, 2021; Pan et al., 2022). Polyethylene (PE), accounting for ~60% of plastic waste, represents both an environmental challenge and an opportunity-its hydrogen-rich structure makes it an ideal candidate for thermochemical treatment. However, conventional PE pyrolysis suffers from limitations in product control and energy efficiency (Li et al., 2021; Rahman et al., 2021; Rathnayake et al., 2021; Wang et al., 2021). Recent studies have demonstrated the significant potential of CE-PE co-pyrolysis in overcoming the inherent drawbacks of single-feedstock pyrolysis (Liu et al., 2020; Vanapalli et al., 2021). Yuan et al. (2018) conducted a comprehensive thermal analysis of CE-PE co-pyrolysis using thermogravimetry-mass spectrometry (TG-MS) and pyrolysis-gas chromatography-mass spectrometry (Py-GC/MS), revealing enhanced volatile release at specific feed ratios. The mechanism involves bidirectional enhancement: PE-derived hydrogen promotes CE decomposition, while CE-derived oxygen--containing species facilitate PE chain scission. When the CE:PE ratio is below 1:1, oxygenate formation is suppressed, and hydrocarbon production is enhanced. Xie et al. (2021)employed response surface methodology to establish quantitative correlations between reaction temperature and optimized hydrocarbon yields, demonstrating increased production of C5-28 hydrocarbons at elevated temperatures. Further mechanistic investigations by Gunasee et al. (2017) showed an 83% improvement in energy recovery efficiency via enhanced char-PE interactions compared to individual component pyrolysis. However, due to the stark differences in pyrolysis mechanisms—CE being rich in oxygen-containing functional groups and PE primarily composed of hydrocarbon chains—the co-pyrolysis process exhibits complex product distributions and poor selectivity. To improve the yield and quality of target products, the introduction of catalysts to regulate reaction pathways becomes imperative.

The introduction of catalysts into the co-pyrolysis process demonstrates remarkable potential for enhancing product selectivity and quality. Current catalysts employed in biomass-plastic co-pyrolysis are broadly categorized into microporous zeolites, mesoporous materials, metal oxides, and composite catalysts (Wachs, 2005; Guda and Toghiani, 2016). Zhao et al. (2019) investigated the performance of HZSM-5 catalyst in CE-PE co-pyrolysis, revealing that HZSM-5 enhances aromatic production by promoting Diels-Alder reactions. However, Mullen et al. (2018) identified a critical limitation of HZSM-5: while effective in deoxygenation and aromatic formation, it consumes hydrogen from already hydrogen-deficient biomass feedstocks, leading to reduced hydrocarbon yields and rapid catalyst deactivation via coking. In contrast, mesoporous materials such as MCM-41 and SBA-15, with their larger pore sizes and superior mass transfer properties, often exhibit insufficient cracking activity due to their relatively weak acidity. Composite catalysts incorporating multiple active components have demonstrated promising performance; however, their complex preparation processes and high costs hinder industrial scalability. Metal oxide catalysts have recently demonstrated unique advantages, particularly highlighting the superior performance of iron oxide (Fe_2O_3) in biomass-plastic co-pyrolysis system. Song et al. (Song et al., 2020) conducted thermogravimetric analyses revealing that Fe_2O_3 incorporation reduces the activation energy of municipal solid waste pyrolysis to 150.18 kJ/mol while simultaneously optimizing the pyrolysis product distribution. Li et al. (2023) developed a novel Fe_2O_3/Al_2O_3 catalyst that establishes proton transfer channels through the formation of $FeAl_2O_4$ spinel phase, achieving an exceptional hydrogen yield of 50.53 mmol·gplastic^{-1}. Lin's (Lin et al., 2018) research further elucidated Fe_2O_3's distinctive capability to promote aromatic compound formation during wood-polypropylene composite pyrolysis. Nevertheless, the fundamental mechanisms governing Fe_2O_3's catalytic activity in co-pyrolysis system remain inadequately understood, particularly requiring atomic-scale investigation at the molecular level.

Reactive force field molecular dynamics (ReaxFF-MD) simulations have emerged as a pivotal tool for unraveling complex pyrolysis mechanisms. Wang et al. (2021) integrated ReaxFF-MD with density functional theory (DFT) calculations to elucidate CE-PE co-pyrolysis pathways, identifying specific reaction routes where PE-derived radicals interact to form alcohols. Their computational results demonstrated a significant reduction in the activation barrier (16.40-22.66 kJ/mol) for furan alcohol formation compared to pure CE pyrolysis. Xuan et al. (2023) conducted comprehensive mechanistic studies on the role of H and C_nH_m fragments from PE in enhancing oil/gas yields, establishing optimal synergistic material ratios. Through investigations of PE interactions with three major biomass components (CE, HC, LG), Wei et al. (2023) revealed that CE promotes accelerated decomposition of oxygen-free carbon into valuable hydrocarbon products. Feng et al. (2024) through ReaxFF molecular dynamics simulations combined with experiments, the three-stage sintering mechanism of Fe_2O_3 particles at 973–1273 K was revealed, showing that elevated temperature promotes atomic diffusion, particularly Fe surface atoms enrich to the neck region, leading to enhanced sintering, with simulation results in good agreement with experiments, indicating that suppressing atomic diffusion is key to improving anti-sintering performance. Despite these advances, existing ReaxFF-MD studies have not fully deciphered Fe_2O_3's catalytic mechanisms in CE-PE co-pyrolysis system.

In this study, we aim to systematically and comprehensively explore the influence of temperature and Fe_2O_3 catalysts on the CE-PE co-pyrolysis using the ReaxFF-MD method. Furthermore, the study seeks to elucidate the underlying mechanism by which the introduction of the catalyst affects the co-pyrolysis process. The findings will provide theoretical guidance for future catalyst development and the efficient resource utilization of biomass and plastics.

2. Computational methods

2.1. Simulation methodology

This study employs the ReaxFF molecular dynamics (ReaxFF-MD) simulation method to investigate the reaction mechanism of the catalytic co-pyrolysis system involving CE, polyethylene PE, and Fe_2O_3. ReaxFF is parameterized based on bond order, enabling it to describe the formation, dissociation, and transformation of chemical bonds during chemical reactions (Feng et al., 2021). The total energy of the system is calculated using the following equation (Kimberly Chenoweth, 2008):

$$E_{system} = E_{bond} + E_{over} + E_{angle} + E_{tors} + E_{vdWaals} + E_{Coulomb} + E_{other} \quad (1)$$

where E_{system} encompasses both bonded and non-bonded interactions. Bonded interactions include bond energy (E_{bond}), overcoordination energy (E_{over}), undercoordination energy (E_{under}), lone pair energy (E_{lp}), valence angle energy (E_{val}), and torsion angle energy (E_{tor}). Non-bonded

interactions consist of van der Waals energy ($E_{vdWaals}$) and Coulombic energy ($E_{Coulomb}$). Bonded interactions are based on the bond order ($BO_{i,j}$), which can be expressed as:

$$BO_{ij} = BO_{ij}^{\sigma} + BO_{ij}^{\pi} + BO_{ij}^{\pi\pi} = \exp\left[p_{bo1}\left(r_{ij}/r_0^{\sigma}\right)^{p_{bo2}}\right] + \exp\left[p_{bo3}\left(r_{ij}/r_0^{\pi}\right)^{p_{bo4}}\right] + \exp\left[p_{bo5}\left(r_{ij}/r_0^{\pi\pi}\right)^{p_{bo6}}\right] \quad (2)$$

where r_{ij} represents the distance between atoms i and j. The p_{bo}-term is an empirical parameter used to calculate the bond order (BO_{ij}). Contributions from σ-bonds, π-bonds, and double π-bonds differ, reflecting their distinct chemical characteristics. By directly calculating the bond order for every atom pair, the model facilitates smooth transitions between non-bonded states and various bonded states (single, double, or triple bonds) during chemical reactions.

The ReaxFF force field exhibits high accuracy because its parameters are trained using quantum mechanics (QM) calculations (Mao et al., 2017). During the development of the ReaxFF force field, a training set was assembled, which included atomic energetics derived from density functional theory (DFT) calculations, including optimized geometries, bond stretching energies, angle bending energies, reaction potential energies, equations of state, and charge distributions (Russo and van Duin, 2011; Li et al., 2021). It has been reported that the ReaxFF-MD simulation method has been widely applied across multiple fields, including fuel combustion (Kimberly Chenoweth, 2008; Bhoi et al., 2014; Feng et al., 2024), pyrolysis (Wei et al., 2022; Yin et al., 2024), and metal oxidation (Zou et al., 2015; Feng et al., 2021).

2.2. Model construction

Cellulose $(C_6H_{10}O_5)_n$, a linear polysaccharide polymer, consists of hundreds of glucose units linked by β-1,4-glycosidic bonds. Polyethylene $(C_2H_4)_n$, on the other hand, is a high-molecular-weight plastic formed through the polymerization of ethylene monomers (Zheng et al., 2016). Depending on the polymerization method and molecular weight, polyethylene can be classified into high-density polyethylene (HDPE), low-density polyethylene (LDPE), linear low-density polyethylene (LLDPE), and ultra-high-molecular-weight polyethylene (UHMWPE) (Wang et al., 2021). In this study, low-density polyethylene (LDPE) was selected as the representative model for PE. Initially, molecular models of 1,4-β-D-glucopyranose monomer and ethylene monomer were constructed, as illustrated in Fig. 1(a) and (b), respectively. Based on these monomer models, polymerization degrees of 10 and 40 were employed to successfully generate the CE and PE polymer chains, respectively. For the catalytic component, an Fe_2O_3 cluster model was developed by extending the α-Fe_2O_3 unit cell, resulting in a spherical nanoparticle with a diameter of approximately 2 nm, composed of 168 iron atoms and 250 oxygen atoms (Fig. 1(c) and (d)). To ensure structural reliability, all constructed polymer chains underwent energy minimization to eliminate local stresses and enhance conformational stability. Additionally, the Fe_2O_3 nanocluster was subjected to thorough relaxation under isothermal conditions at 300 K to achieve a thermodynamically stable initial configuration prior to simulation.

Building upon these initial models, this study established two distinct simulation systems to systematically investigate the CE-PE co-pyrolysis mechanism and its catalytic counterpart mediated by Fe_2O_3. Fig. 1(e)

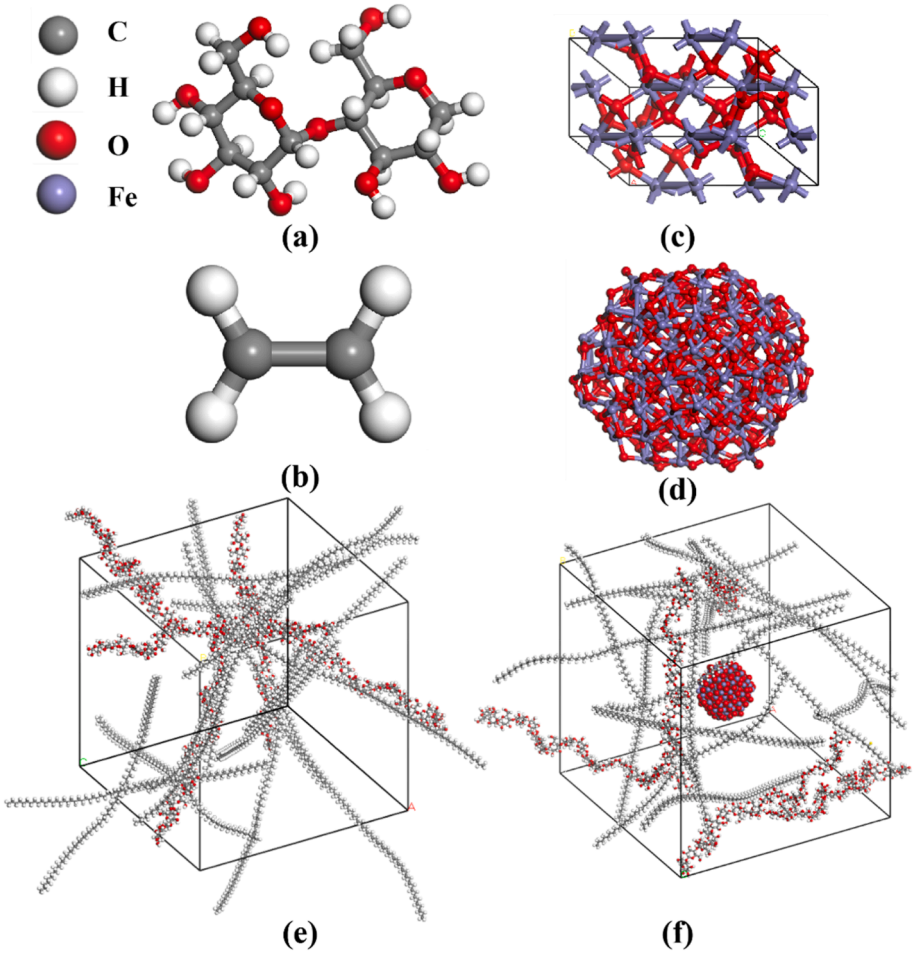


Fig. 1. Molecular models: (a) CE monomer, (b) PE monomer, (c) α- Fe_2O_3 unit cell, (d) Fe_2O_3 cluster. Pyrolysis system models: (e) CE-PE co-pyrolysis system, (f) CE-PE- Fe_2O_3 catalytic co-pyrolysis system (Color scheme: gray - carbon, white - hydrogen, red - oxygen, purple - iron).

represents a non-catalytic co-pyrolysis system with a 1:1 mass ratio of CE to PE, constructed as a cubic periodic box (density = 0.1 g/cm^3) containing 5 CE chains and 15 PE chains (totaling 5740 atoms: $C_{1800}H_{3440}O_{500}$) within an 82 Å edge-length unit cell. Periodic boundary conditions were applied in all directions to eliminate surface effects, followed by thorough geometric optimization to achieve a stable configuration. The catalytic system (Fig. 1(f)) maintains identical polymer chain numbers and density while incorporating the Fe_2O_3 nanocluster, yielding an expanded atomic system (6158 atoms: $C_{1800}H_{3440}O_{750}Fe_{168}$) for probing the catalyst's mechanistic role.

In this study, the present simulations were still performed using a fixed simulation density, CE:PE ratio, box dimension, and Fe_2O_3 cluster size. Therefore, the conclusions should be interpreted as being supported within the tested CE:PE ratio range and the selected model configuration. Future work should systematically assess the sensitivity of product distribution, bond evolution, oxygen transfer behavior, and catalytic effects to simulation density, box dimension, and Fe_2O_3 cluster size.

2.3. Simulation parameters

For the ReaxFF-MD simulations of the established system in this study, the LAMMPS software and the Reax/c module were utilized for analysis (Aktulga et al., 2012). At each time step, the charge equilibration (QEq) method was applied to naturally capture changes in oxidation states and maintain charge neutrality throughout the simulation. The C/H/O/Fe reactive force field was employed to describe the chemical reactions, as this force field has been validated in previous studies. Specifically, Shin et al. (2015) used it to investigate the pyrolysis of butane over chromium oxide/pyrite catalysts, while Zhan et al. (2024) applied it to study the water vapor gasification of lignin dimer catalyzed by iron and its oxides. Therefore, this study adopts the same ReaxFF force field to explore the reaction processes and mechanisms of the catalytic CE-PE co-pyrolysis under the influence of Fe_2O_3 catalysis.

The constructed system models were converted into data files compatible with the LAMMPS molecular simulation software, with corresponding parameters configured for simulation. Prior to formal pyrolysis simulation, the pyrolysis system models underwent low-temperature annealing at 300-500 K for 100 ps under the NVT ensemble to minimize system energy and enhance structural stability. Following preliminary tests across multiple pyrolysis temperature conditions, five temperature points ranging from 1800 to 2600 K at 200 K intervals were ultimately selected for isothermal pyrolysis simulations of both co-pyrolysis and catalytic co-pyrolysis systems, each conducted for 1000 ps under the NVT ensemble with a time step of 0.2 fs. Elevated temperatures were employed to accelerate pyrolysis reactions within the nanosecond-scale time window accessible to ReaxFF-MD. (Paajanen and Vaari, 2017; Xuan et al., 2023), the high-temperature simulation in this paper is an accelerated atomic-scale sampling method, which is used to compare the early bond decay, radical evolution, oxygen transfer and short-time fragment reactions in CP system with CCP system under the same conditions.

3. Results and analysis

3.1. Pyrolysis product analysis

3.1.1. Distribution of pyrolysis products by carbon number

To systematically investigate the product distribution characteristics of both the CE-PE co-pyrolysis (CP) system and the CE-PE-Fe_2O_3 catalytic co-pyrolysis (CCP) system under varying temperature conditions, the pyrolysis products were quantitatively analyzed and classified into four distinct categories based on their carbon number: gaseous products (C1-C4), light liquid products (C5-C19), heavy liquid products (C20-C39), and char products (C40+) (Zheng and Li, 2024). The temporal evolution of these product categories across five temperature conditions (1800-2600 K at 200 K intervals) is comprehensively presented in Fig. 2, where solid and dashed lines respectively represent the CP and CCP systems, with all subplots maintaining consistent y-axis scaling for direct comparability.

The results demonstrate significant temperature dependence in product distribution. As temperature increased, C1-C4 products achieved their peak concentrations faster and at higher values, as illustrated in Fig. 2(a). At 1800-2200 K, C1-C4 product quantities increased monotonically with pyrolysis time before reaching equilibrium at 1000 ps, whereas at 2400-2600 K they exhibited rapid initial growth followed by gradual decline due to secondary reactions converting small molecules into C5-C19 and C20-C39 products. Consequently, the C5-C19 and C20-C39 product profiles (Fig. 2(b)-(c)) showed opposite trends, increasing then stabilizing at lower temperatures (1800-2200 K), but displaying more complex rise-fall-rise patterns at higher temperatures (2400-2600 K). As shown in Fig. 2(d), within the selected elevated-temperature range of 1800-2600 K, C40+ species rapidly decreased during the early pyrolysis stage, indicating accelerated fragmentation of CE and PE chains under the present high-temperature ReaxFF-MD conditions. Besides, the threshold-sensitivity analysis shows that the absolute product counts are affected by the molecular-identification criteria, as illustrated in Supplementary Material Table 1. However, the distribution trend of products based on the number of carbon and the CP/CCP system comparisons remain unchanged under reasonable variations in bond-order thresholds.

The catalytic effects of Fe_2O_3 manifested in two primary aspects: (1) Accelerated degradation of C40+ components in CCP system versus CP system at 1800-2200 K, confirming Fe_2O_3's promotion of initial polymer chain cleavage; (2) Temperature-dependent selectivity shifts where CP system favored C5-C19 production at 1800-2000 K, while CCP system exhibited enhanced selectivity for these products at 2200-2600 K, demonstrating stronger catalytic regulation at elevated temperatures. Lin et al. (Lin et al., 2018) investigated the catalytic pyrolysis of wood-polypropylene composite (WPP) using Py-GC/MS methodology in the presence of four metal oxide catalysts (ZnO, CaO, Fe_2O_3, and MgO). Their results demonstrated that the incorporation of metal oxides significantly enhanced polyolefin cracking efficiency, consequently leading to increased yields of C4-C24 products. This finding is qualitatively consistent with our ReaxFF-MD observation that the CCP system favors the formation of C5-C19 products under certain high-temperature conditions, suggesting a similar tendency of metal oxides to influence intermediate-carbon-number product formation during biomass-plastic co-pyrolysis.

Furthermore, this study conducted a comparative analysis of mass percentage variations for different carbon-number products in both CP and CCP systems across various pyrolysis temperatures, as shown in Fig. 3, where panel (a) represents results at 500 ps and panel (b) at 1000 ps. Comparative examination reveals that within the 1800-2200 K range, both systems exhibit significantly higher mass percentages of heavy liquid products at 500 ps compared to 1000 ps, while gas products demonstrate the opposite trend. In contrast, at elevated temperatures ranging from 2400 to 2600 K, the product evolution follows an inverse pattern. This phenomenon clearly demonstrates that under relatively lower temperatures (1800-2200 K), the pyrolysis proceeds at a diminished reaction rate, with the initial 500 ps primarily involving the fragmentation of macromolecular chains. During this stage, the decomposition remains incomplete, resulting in a predominant formation of heavy liquid products. As the pyrolysis duration extends to 1000 ps, the mass fraction of heavy liquid products decreases significantly while that of gaseous products exhibits a corresponding increase, attributable to the progressive decomposition of intermediate products into smaller molecular gases. Conversely, at higher temperatures (2400-2600 K), the accelerated pyrolysis reaction kinetics facilitate rapid scission of macromolecular chains during the initial stages, directly yielding considerable quantities of small molecular products. Simultaneously, larger molecular species (light and heavy liquid products)

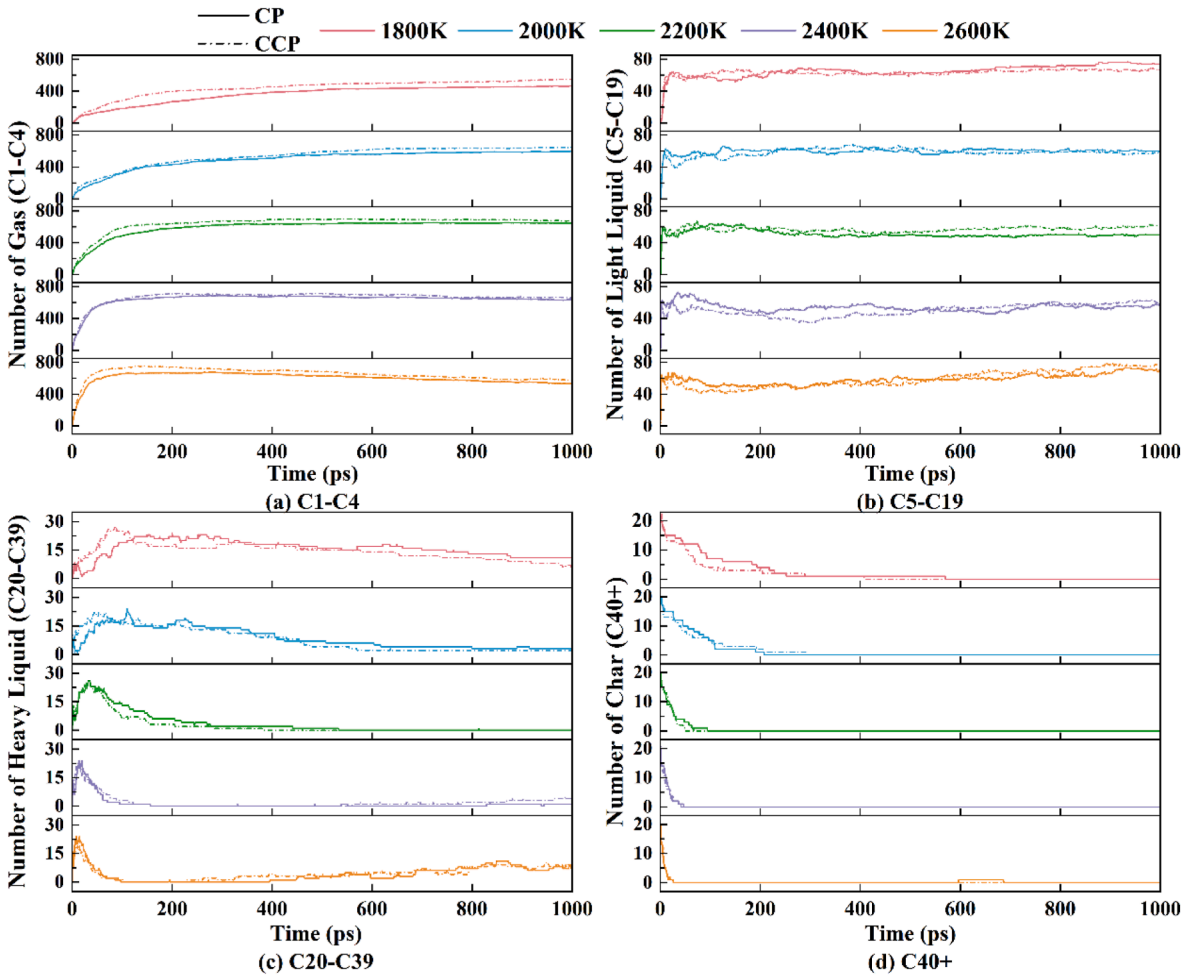


Fig. 2. Temporal evolution of pyrolysis product quantities in CP and CCP systems: (a) C1-C4, (b) C5-C19, (c) C20-C39, and (d) C40+ (Results from ReaxFF-MD simulations at 1800 -2600 K for 1000 ps).

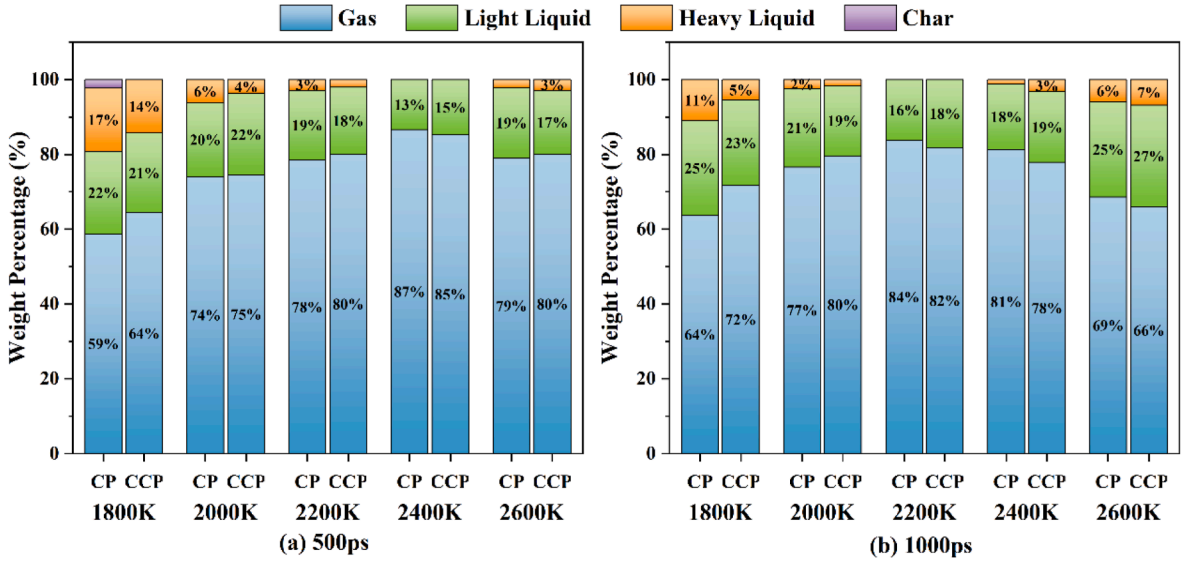


Fig. 3. Mass percentage distribution of pyrolysis products in CP and CCP systems at 500 ps and 1000 ps: (a) 500 ps, (b) 1000 ps (Results from ReaxFF-MD simulations at 1800-2600 K for 1000 ps).

through the recombination of small molecules or free radicals during the later stages of pyrolysis.

The temperature-dependent selectivity control becomes particularly evident in Fig. 3(b). Both systems display pronounced thermal response

patterns: gas product mass fractions initially increase before decreasing, peaking at 2200 K (CP: 84%; CCP: 82%), while light and heavy liquid products show inverse trends, reaching minima at 2200 K (CP: 16%, 0%; CCP: 18%, 0%). This transition suggests that C-C bond cleavage is more dominant below 2200 K, whereas at higher temperatures the product distribution is increasingly influenced by secondary reactions, including radical recombination and fragment-growth events. Notably, at 1800 and 2000 K, CCP systems produce higher gas yields, demonstrating that Fe_2O_3's catalytic enhancement of low-temperature cracking while CP system generate more light liquids. However, between 2200 and 2600 K, CCP system preferentially produce light liquids, with CP systems yielding more gases observations fully consistent with the previously discussed quantitative trends.

3.1.2. Statistical analysis of small-molecule pyrolysis products

Both systems generate various small-molecule products during pyrolysis, including inorganic gases (H_2O, H_2, CO, CO_2) and oxygenated compounds. Among these, glycolaldehyde ($C_2H_4O_2$) and formaldehyde (CH_2O) serve as key intermediates and final products. This study quantitatively compares the evolution of these small molecules in both systems. As shown in Fig. 4(a)-(b), the yields of inorganic gases after 1000 ps of pyrolysis exhibit distinct temperature-dependent trends across both systems. Notably, H_2O consistently demonstrates the highest yield at all temperatures, followed by H_2 and CO, while CO_2 maintains the lowest production levels. The yields of H_2O, H_2, and CO increase monotonically with temperature, reaching maxima at 2600 K, whereas CO_2 production remains consistently low.

In comparison to the CP system, the CCP system demonstrates significantly increased yields of H_2O and CO, while showing reduced H_2 production. Furthermore, the disparity in inorganic gas yields between the two systems becomes more pronounced with increasing temperature. This phenomenon can be mechanistically explained as follows: The formation of H_2O is promoted through the reaction between hydrogen radicals (H) generated from polyethylene pyrolysis and cellulose-derived alcohols (R-OH), following the equation: R-OH + H → R + H_2O. Additionally, partial lattice oxygen from Fe_2O_3 migrates and combines with hydrogen radicals in the system to form additional H_2O. This process simultaneously consumes hydrogen sources that would otherwise contribute to H_2 formation, resulting in higher H_2O and lower H_2 yields in the CCP system compared to the CP system. Regarding CO production, the yield primarily depends on carbon and oxygen sources. The carbon originates from the decomposition of cellulose and polyethylene, where more fragmented carbon species lead to greater CO formation. The oxygen supply derives not only from cellulose decomposition but also benefits from the lattice oxygen provided by Fe_2O_3, resulting in higher CO yields in the CCP system. At lower temperatures, CO production remains relatively low, but increases with rising temperature, indicating that elevated temperatures promote both the decomposition of long-chain molecules and the mobility of Fe_2O_3 lattice oxygen, thereby facilitating CO generation.

These findings are qualitatively in line with the work of Song et al. (Song et al., 2020), who investigated iron-based catalysts (iron ore and iron oxide) for municipal waste pyrolysis containing biomass-plastic mixtures. Their GC-MS/GC analyses demonstrated that both catalysts reduced heteroatomic compounds in tar while increasing H_2 and CO yields, consistent with our ReaxFF-MD observations of elevated H_2O and CO production in CCP systems. However, this comparison should be regarded as qualitative support for a similar catalytic tendency rather than direct validation of the specific CCP system reaction mechanism proposed in this study.

Fig. 4(c)-(f) illustrates the temporal and thermal evolution of two principal oxygenated intermediates, CH_2O and $C_2H_4O_2$, in both systems. Within the CP system, CH_2O formation exhibits distinct temperature dependence: its yield increases with temperature from 1800 to 2000 K, peaks at 2200 K, and subsequently declines to minimum values at 2600 K. This non-monotonic behavior reflects CH_2O's dual role as both a primary product from cellulose chain scission and a reactant in secondary reactions. Particularly under 2400 and 2600 K conditions, CH_2O concentrations demonstrate characteristic unimodal profiles, reaching maxima at approximately 100 ps before decreasing due to participation in recombination reactions ($CH_2O + HO \rightarrow CH_3O_2$; $CH_2O + CH_3 \rightarrow C_2H_5O$). While the CCP system ultimately achieves similar terminal CH_2O yields after 1000 ps pyrolysis, its distinctive behavior at 2600 K—featuring rapid CH_2O accumulation within 100 ps followed by accelerated depletion— reveals Fe_2O_3's bifunctional catalysis: simultaneously enhancing CH_2O generation through promoted cellulose dissociation while accelerating its subsequent conversion.

As depicted in Fig. 4(e) and (f), both systems display monotonically decreasing $C_2H_4O_2$ yields with increasing temperature, though with transient maxima whose temporal positions exhibit strong thermal correlation (peak appearance advances with temperature). The CCP system demonstrates markedly faster $C_2H_4O_2$ consumption rates compared to CP, evidencing Fe_2O_3's catalytic promotion of $C_2H_4O_2$ decomposition ($C_2H_4O_2 \rightarrow H_2O + C_2H_2O$).

3.2. Bond evolution and pyrolysis kinetic analysis

The above product distribution analysis reveals the dynamic changes of different product categories in the CP system and the CCP system at various temperatures. To gain deeper insight into the microscopic mechanisms underlying these macroscopic product distributions, we further analyze the dynamic evolution of C-C, C-H, and C-O bonds. The breaking and recombination of bonds directly determine the formation pathways and final distributions of products. Therefore, by tracking the dynamic changes of these key chemical bonds, we can uncover the details of reaction kinetics and thereby connect the macroscopic product distributions with the microscopic bond dynamics.

3.2.1. Analysis of C-C, C-H, and C-O bond evolution

To elucidate the bond cleavage and recombination mechanisms in both CP and Fe_2O_3-catalyzed CCP systems, we systematically investigated the temporal evolution of C-C, C-H, and C-O bonds in CE and PE at different temperatures (1800, 2200, and 2600 K). As shown in Fig. 5, all bond types exhibit rapid initial depletion, with higher temperatures accelerating bond cleavage rates, confirming that elevated temperatures significantly enhance CE and PE pyrolysis. Notably, at 2600 K, the C-C bond count reaches a minimum before rebounding, directly correlating with the recombination of small molecules into higher carbon-number products (C5-C19 and C20-C39). This observation aligns with the increased mass fractions of light and heavy liquid products discussed in Section 3.1.1 Comparative analysis reveals the CCP system exhibits superior C-C and C-H bond cleavage efficiency relative to the CP system under identical conditions, demonstrating Fe_2O_3's catalytic efficacy in promoting polymer chain scission. However, closer examination shows the CCP system displays reduced C-O bond cleavage, which stems from Fe_2O_3's dual functionality: (1) released lattice oxygen reacts with carbon radicals during pyrolysis, thereby suppressing C-O bond cleavage. (2) facilitating oxygenated intermediate formation through oxygen transfer. This mechanistic insight confirms Fe_2O_3's bifunctional role - not only accelerating C-C/C-H bond rupture but also regulating product distribution via oxygen donation, providing crucial theoretical guidance for optimizing reaction pathways.

3.2.2. Analysis of Fe-O bond evolution

In ReaxFF-MD simulations, the atomic indices remain continuous and unchanged throughout the process. This allows for tracking molecular composition by labeling atoms of distinct components in the initial model and identifying their molecular affiliations post-reaction. To elucidate the dynamic evolution of Fe_2O_3 catalysts during pyrolysis, this study quantified the temporal variations in Fe-O bond counts within the CCP system at different temperatures. As illustrated in Fig. 6, the Fe-O bonds were categorized into two types based on oxygen origins:

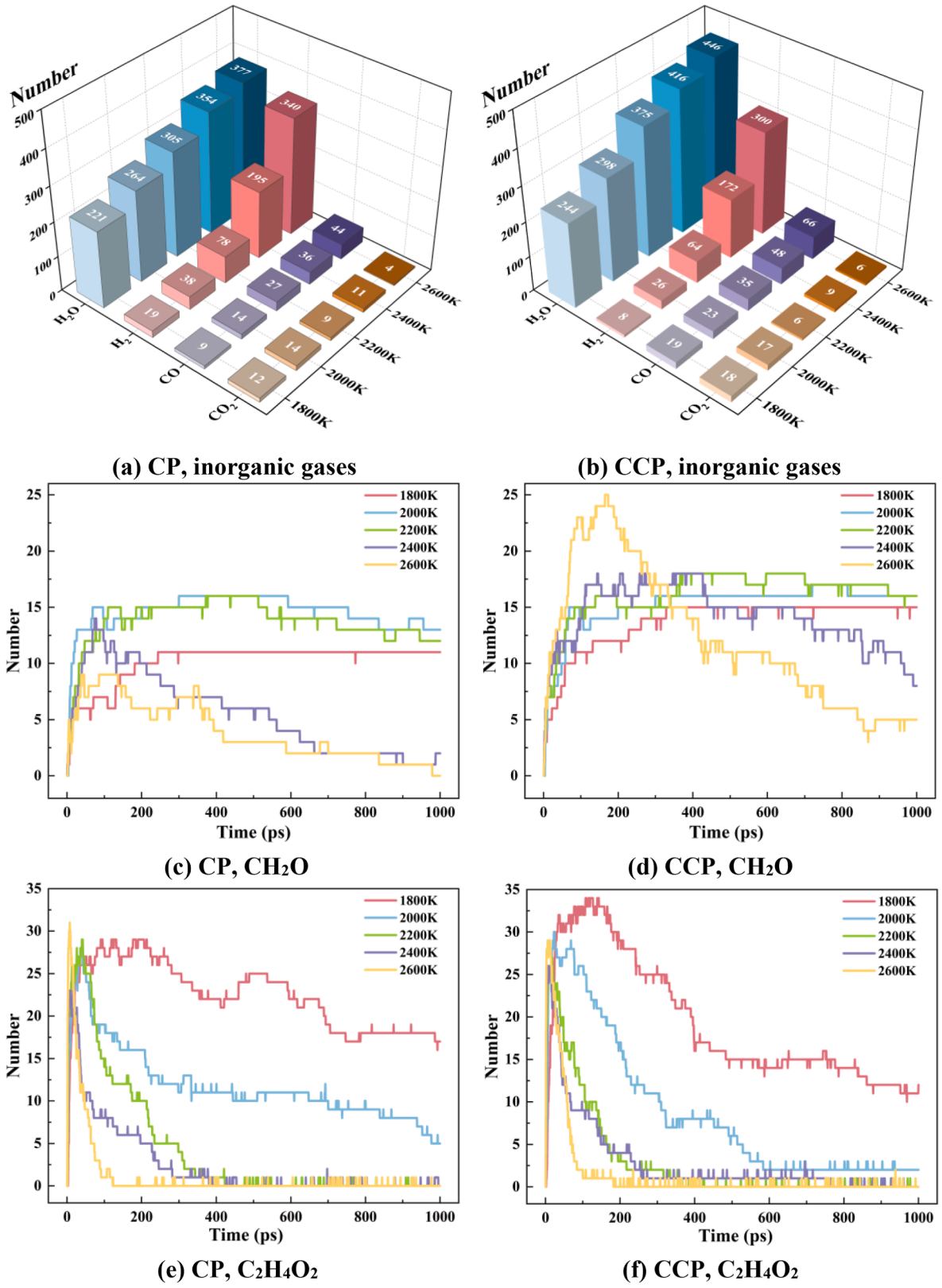


Fig. 4. Evolution trends of inorganic gases and CH_2O and $C_2H_4O_2$ in CP and CCP systems: (a)CP, inorganic gases; (b)CCP, inorganic gases; (c) CP, CH_2O; (d) CCP, CH_2O; (e) CP, $C_2H_4O_2$; (f) CCP, $C_2H_4O_2$.

red columns represent Fe-O bonds where oxygen derives from the lattice oxygen of the Fe_2O_3 catalyst (Lattice-O), while blue columns denote those involving reactive oxygen from cellulose decomposition (CE-O). Initial-state analysis (t_1) confirmed that all Fe-O bonds exclusively comprised Lattice-O. As pyrolysis progressed, Lattice-O exhibited a monotonic decrease, whereas CE-O gradually increased. Concurrently, the total Fe-O bond count diminished, indicating that Lattice-O continuously detaches from the catalyst surface to participate in reactions,

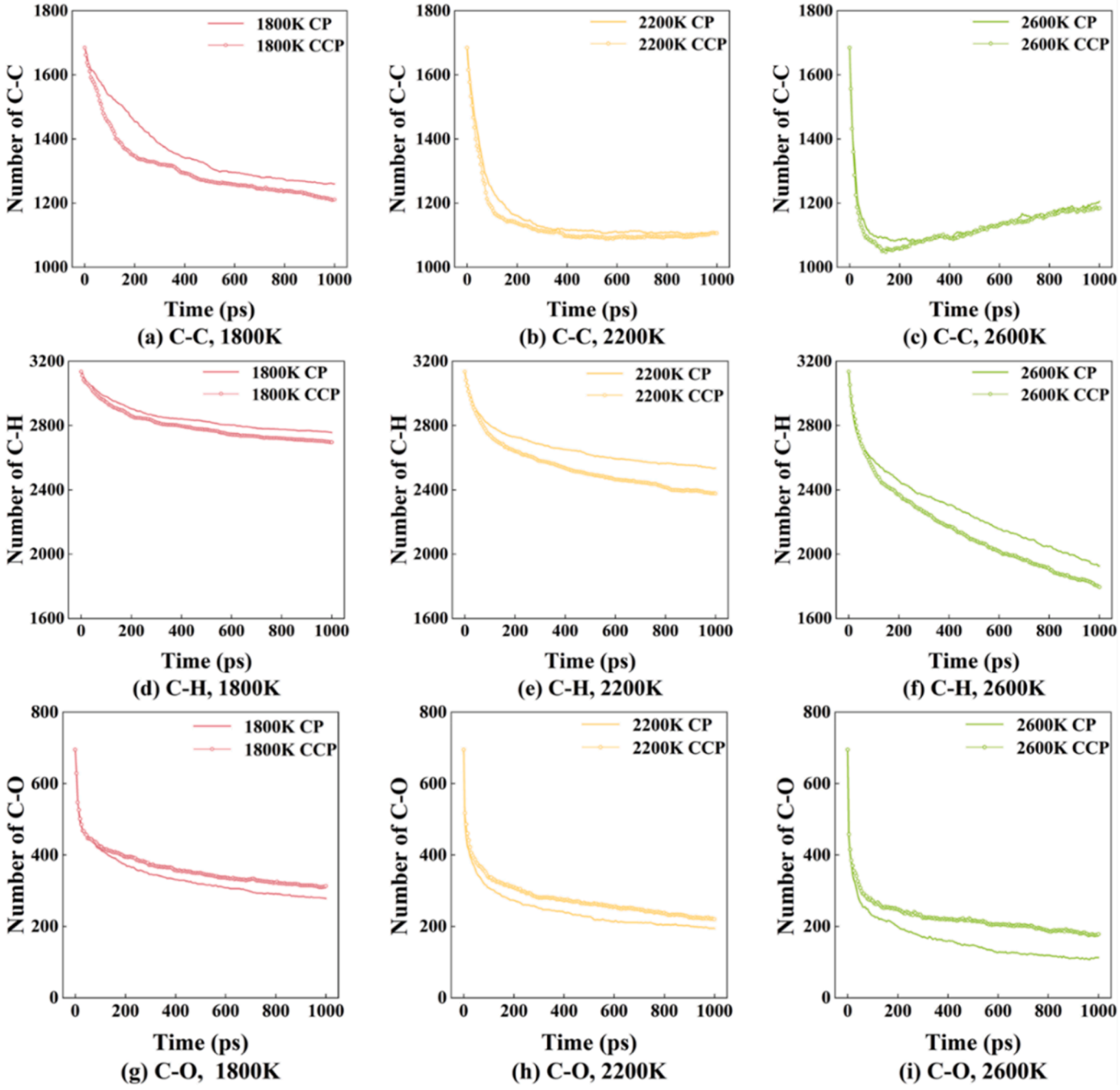


Fig. 5. Evolution trends of C-C, C-H, and C-O bond counts in CP and CCP systems as functions of time and temperature: (a) C-C bonds at 1800 K, (b) C-C bonds at 2200 K, (c) C-C bonds at 2600 K, (d) C-H bonds at 1800 K, (e) C-H bonds at 2200 K, (f) C-H bonds at 2600 K, (g) C-O bonds at 1800 K, (h) C-O bonds at 2200 K, (i) C-O bonds at 2600 K.

reducing red column heights, while liberated lattice oxygen is replaced by reactive oxygen from cellulose pyrolysis, forming new Fe-O bonds with Fe, increasing blue column heights. This manifests a dynamic process involving lattice-oxygen migration, oxygen exchange, and the formation of local oxygen-deficient Fe sites on the catalyst surface. Notably, these trends intensified with rising pyrolysis temperatures: higher temperatures accelerated Lattice-O consumption and enhanced CE-O incorporation, demonstrating that elevated temperatures simultaneously promote lattice oxygen release and the ingress of cellulose-derived oxygen into the catalyst.

Additionally, this study investigated the dynamic structural evolution of the Fe_2O_3 catalyst during pyrolysis by tracking the changes in the O/Fe stoichiometric ratio of the Fe_2O_3 cluster, as illustrated in Supplementary Material Fig. 1. The initial Fe_2O_3 catalyst cluster model consisted of 168 Fe atoms and 250 O atoms, yielding an O/Fe stoichiometric ratio of 1.488 (~1.5), consistent with the theoretical ratio of trivalent iron oxide. Notably, the initial simulated O/Fe ratio was as high as 3.3, significantly deviating from the theoretical value. This anomaly arose from the adsorption of cellulose molecular chains onto the Fe_2O_3 cluster surface, causing some oxygen atoms from cellulose to be erroneously identified as part of the catalyst, thereby artificially inflating the detected O count beyond the actual Fe_2O_3 oxygen content. However, within approximately 2 ps of pyrolysis initiation, the adsorbed cellulose chains rapidly dissociated, and the O/Fe ratio promptly returned to the

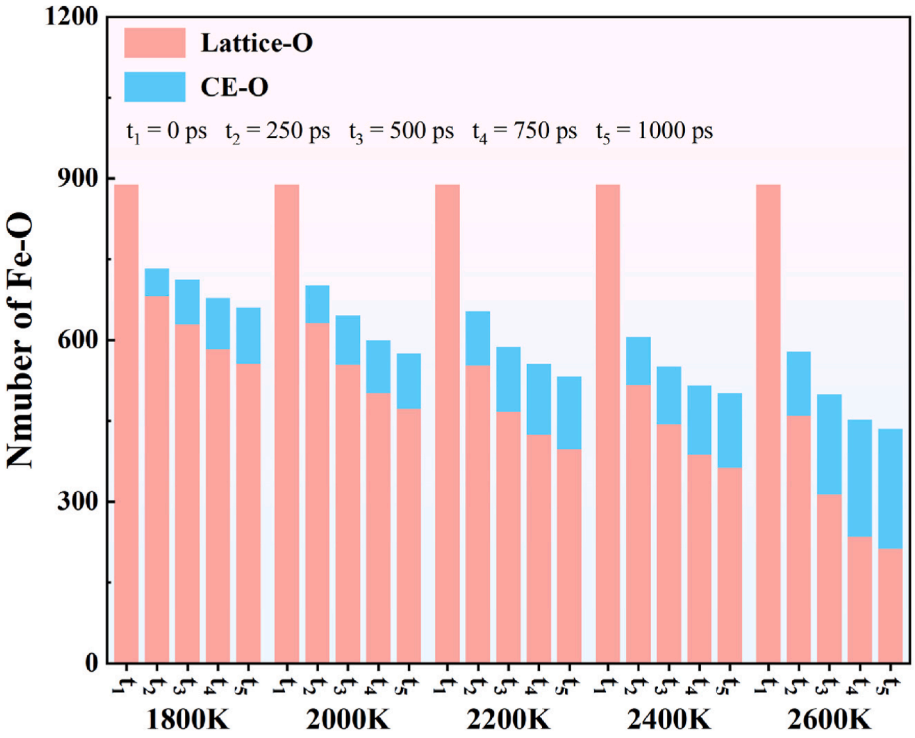


Fig. 6. Evolution trends of Fe-O bond counts in the CCP system as functions of temperature and time, along with the origin of oxygen.

theoretical range of ~1.5. Consequently, this transient anomaly was therefore disregarded in subsequent analyses to ensure data accuracy. As pyrolysis progressed, the O/Fe ratio exhibited a continuous decline, with a pronounced temperature dependence: higher pyrolysis temperatures resulted in lower O/Fe ratios. This trend is consistent with the reduction in Fe-O bond counts and supports the occurrence of lattice-oxygen loss from the Fe_2O_3 catalyst during pyrolysis. Particularly, elevated temperatures promoted lattice-oxygen loss and increased the population of oxygen-deficient, low-coordinated Fe sites, suggesting a greater tendency toward oxygen-vacancy like defect formation.

3.2.3. *Pyrolysis kinetic analysis*

The pyrolysis reaction kinetics was primarily investigated based on the Arrhenius equation (Bui et al., 2016). The kinetic model enables analysis of the pyrolysis rates of reactants during thermal decomposition, providing key parameters such as activation energy and pre-exponential factor. Unlike complex multi-step models, the pyrolysis kinetics of polymers like biomass typically follows a single-reaction mechanism. In this study, the progress of pyrolysis reactions was characterized by monitoring the temporal evolution of C-C and C-H bonds (Chen et al., 2017; Hu et al., 2021). The rate constant k was determined using the following first-order rate law equation (Si et al., 2019; Chen et al., 2021):

$$\ln N_0 - \ln N_t = kt \tag{3}$$

where N_0 and N_t represent the number of C-C and C-H bonds at the initial state and at a given instant, respectively. t represents time, and k is the rate constant. Subsequently, the activation energy and pre-exponential factor are calculated using the following Arrhenius equation, through linear fitting:

$$k = A \exp\left(-\frac{E_a}{RT}\right) \tag{4}$$

where A represents the pre-exponential factor, E_a represents the apparent activation energy, R represents the universal gas constant, and T represents the pyrolysis temperature.

As illustrated in Fig. 7, the rate constants for both systems exhibit a marked increase with rising temperature, indicating an acceleration of pyrolysis rate at elevated temperatures. For the C-C bond-counts decay reaction, the apparent activation energy measures 100.69 kJ/mol in the CP system, while significantly decreasing by 11.9% to 88.72 kJ/mol in the CCP system. Similarly, the apparent activation energy for C-H bond-counts decay shows a reduction from 86.86 to 77.87 kJ/mol in the CCP system, representing a 10.2% decrease. These findings clearly demonstrate that the incorporation of Fe_2O_3 catalyst reduces the apparent activation energy required for both C-C and C-H bond-counts under the selected model, thereby enhancing the overall pyrolysis efficiency. It should be noted that the activation energy calculation method used in this study is based on the decay of C-C and C-H bonds, which is effective for simple reactions. However, in complex multi-step radical networks, composite reactions may lead to deviations in net bond counts, thereby affecting the accuracy of apparent activation energy. Nevertheless, our focus is on the relative reduction of apparent activation energy in the catalytic system rather than the absolute values. By comparing the apparent activation energies of the CCP system and the CP system, we observed that the Fe_2O_3 catalyst significantly lowers the apparent activation energies for C-C and C-H bond-counts decay, indicating a substantial catalytic effect in promoting reaction kinetics.

3.3. *Reaction pathway analysis*

To gain deeper insights into the mechanistic influence of Fe_2O_3 catalyst on the pyrolysis of CE and PE, we systematically analyzed the formation processes and underlying mechanisms of major pyrolysis products. Fig. 8 delineates the reaction pathways for principal products (CH_4, C_2H_2, C_2H_4, CH_2O).

During the initial pyrolysis stage, CE undergoes depolymerization to form low-degree polymerization cellulose intermediates, primarily cellobiose and other C_6-based intermediate compounds collectively termed as active cellulose (AC). As shown in Fig. 8, the formation pathway (Path 1) of methane (CH_4) exhibits significant differences between CCP system and the CP system, primarily in the generation

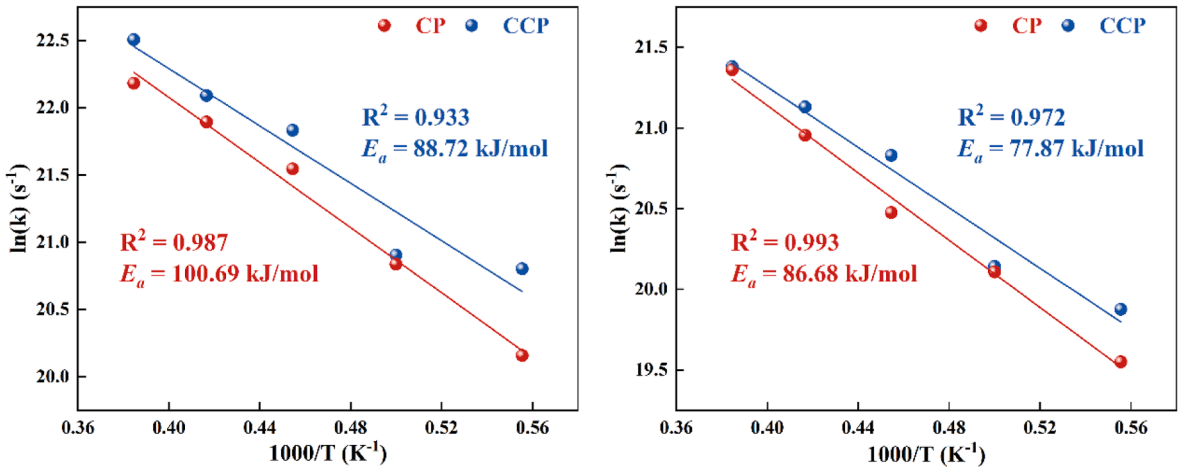


Fig. 7. Apparent activation energies derived from C-C and C-H bond-count decay in CP and CCP systems: (a) C-C bonds, (b) C-H bonds.

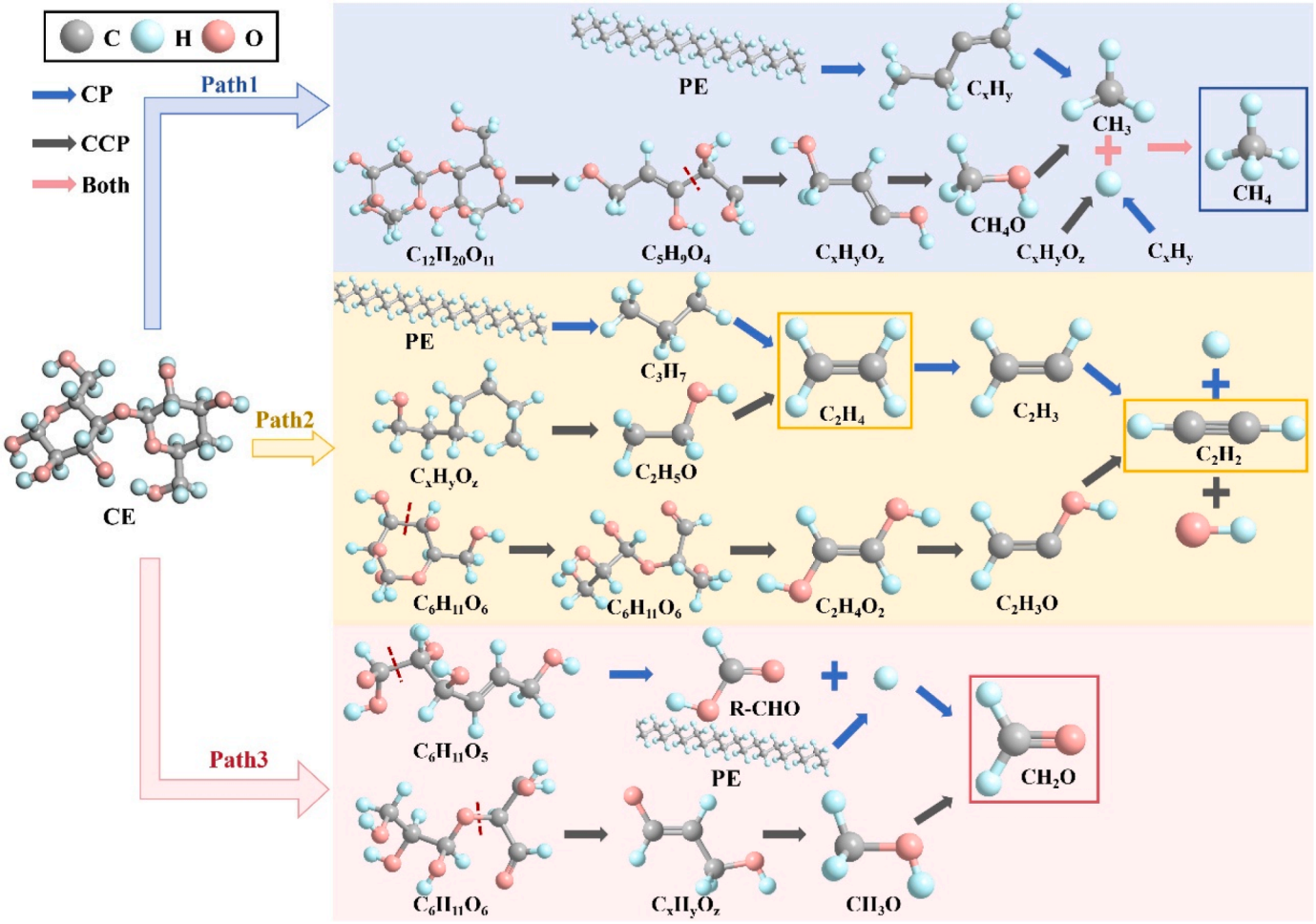


Fig. 8. Reaction pathways of major gaseous products: Path 1 (CH_4), Path 2 (C_2H_2 and C_2H_4), and Path 3 (CH_2O). (Blue arrows: reaction pathways in CP system; black arrows: CCP system; red arrows: common pathways in both systems; gray: carbon; blue: hydrogen; pink: oxygen).

mechanism of the CH_3 radical. In the CP system, CH_3 radicals predominantly form through sequential fragmentation of PE into smaller hydrocarbon fragments (PE → C_xH_y → CH_3). In contrast, the CCP system demonstrates an alternative route where AC undergoes ring-opening via C-C bond cleavage to yield oxygenated intermediates ($C_5H_9O_4$), which subsequently decompose through hydrogen transfer reactions to form CH_4O. Subsequent dehydroxylation of CH_4O generates CH_3 radicals (AC → $C_xH_yO_z$ → CH_4O → CH_3). Ultimately, these CH_3 radicals combine with hydrogen radicals to produce CH_4 ($CH_3 + H \rightarrow CH_4$).

Fig. 8 (Path 2) illustrates the evolution pathways of C_2 products, revealing distinct differences in ethylene (C_2H_4) and acetylene (C_2H_2) formation between the two systems. In the CP system, C_2H_4 primarily forms through PE chain scission into smaller radicals, where the intermediate C_3H_7 dissociates into C_2H_4 and CH_3 (PE → C_3H_7 →

C_2H_4 + CH_3). Conversely, in the CCP system, C_2H_4 generation predominantly originates from dehydroxylation of CE-derived oxygenated intermediates ($C_xH_yO_z$), specifically via the transformation of C_2H_5O (CE → C_2H_5O → C_2H_4 + OH). The formation pathway of C_2H_2 in the CP system proceeds through sequential dehydrogenation of C_2H_4, initially yielding C_2H_3 followed by further hydrogen abstraction (C_2H_4 → C_2H_3 + H → C_2H_2 + H). In contrast, the CCP system follows an alternative route, as shown in the lower section of Path 2, where AC first undergoes ring-opening and C-C bond cleavage to form $C_2H_4O_2$, which subsequently eliminates two hydroxyl groups to produce C_2H_2 (AC → $C_2H_4O_2$ → C_2H_2 + 2OH). Comparative analysis of these distinct reaction pathways demonstrates that the introduction of Fe_2O_3 catalyst facilitates the involvement of oxygenated intermediates in C_2 product formation, thereby altering the product generation routes. These findings elucidate the regulatory role of Fe_2O_3 catalyst in modifying reaction pathways.

Fig. 8 (Path 3) presents the formation pathways of formaldehyde (CH_2O). Since PE contains no oxygen element, CH_2O primarily originates from CE depolymerization, albeit through markedly different mechanisms in the two systems. In the CP system, CH_2O mainly forms through aldehyde group cleavage of oxygenated intermediates ($C_xH_yO_z$), followed by combination with hydrogen radicals generated from PE pyrolysis (R-CHO + H → R + CH_2O). In stark contrast, the CCP system demonstrates an alternative mechanism where oxygenated intermediates first undergo fragmentation to produce methoxy groups (CH_3O), which subsequently convert to CH_2O via dehydrogenation ($C_xH_yO_z$ → CH_3O → CH_2O + H). This distinct divergence in reaction pathways reveals that the introduction of Fe_2O_3 catalyst not only modifies CE depolymerization routes but, more significantly, regulates the evolution processes of oxygen-containing functional groups.

Building upon the simulation results, this study further elucidates the interaction mechanisms among CE, PE, and Fe_2O_3 catalyst. Fig. 9 presents the principal formation pathways of pyrolysis products H_2O and CO under catalytic conditions. The results demonstrate that lattice oxygen on the Fe_2O_3 catalyst surface rapidly captures hydrogen atoms from CE and PE through O-H bond formation. This process not only weakens the C-H bonds in CE and PE but also facilitates the detachment of lattice oxygen from the catalyst surface, generating reactive OH radicals. These radicals subsequently combine with free hydrogen atoms to form H_2O. Regarding CO production, the pathway exhibits similar initial steps to H_2O formation. Hydrogen atoms from CE and PE are first abstracted through O-H bonding, while carbon chains undergo adsorption or cleavage near the catalyst surface to form shorter fragments. The liberated OH groups then react with these fragments to produce hydroxylated intermediates, as exemplified by the $C_4H_{10}O$ intermediate shown in Fig. 9. With continued pyrolysis, these chains undergo further cleavage, with hydrogen elimination from hydroxyl groups yielding C_2H_3O, followed by C-C bond scission to ultimately produce CO and CH_2 (C_4H_{10} + OH → $C_4H_{10}O$ → C_2H_3O → CH_3 + CO). These findings collectively demonstrate that Fe_2O_3 catalyst significantly enhances H_2O and CO generation in the CCP system, consistent with the previously observed increase in their production quantities.

4. Conclusions

This study systematically investigated the catalytic co-pyrolysis mechanism of cellulose (CE) and polyethylene (PE) mediated by iron oxide (Fe_2O_3) catalyst using ReaxFF-MD simulations, with particular focus on elucidating the effects of temperature and catalyst on pyrolysis behavior and reaction mechanisms. The principal conclusions are summarized as follows:

(1) In the catalytic co-pyrolysis system, the cleavage rate of coke products was significantly accelerated at 1800-2200 K, accompanied by higher mass yields of gaseous products compared to the co-pyrolysis system, demonstrating Fe_2O_3's catalytic effect on initial polymer chain scission. At temperatures exceeding 2200 K, the CCP system exhibited enhanced formation of light liquid products, which was associated with the competition between rapid cracking and secondary fragment-growth and recombination reactions under high-temperature conditions.
(2) The incorporation of Fe_2O_3 substantially increased both the quantity and efficiency of C-C and C-H bond-count decay. Kinetic

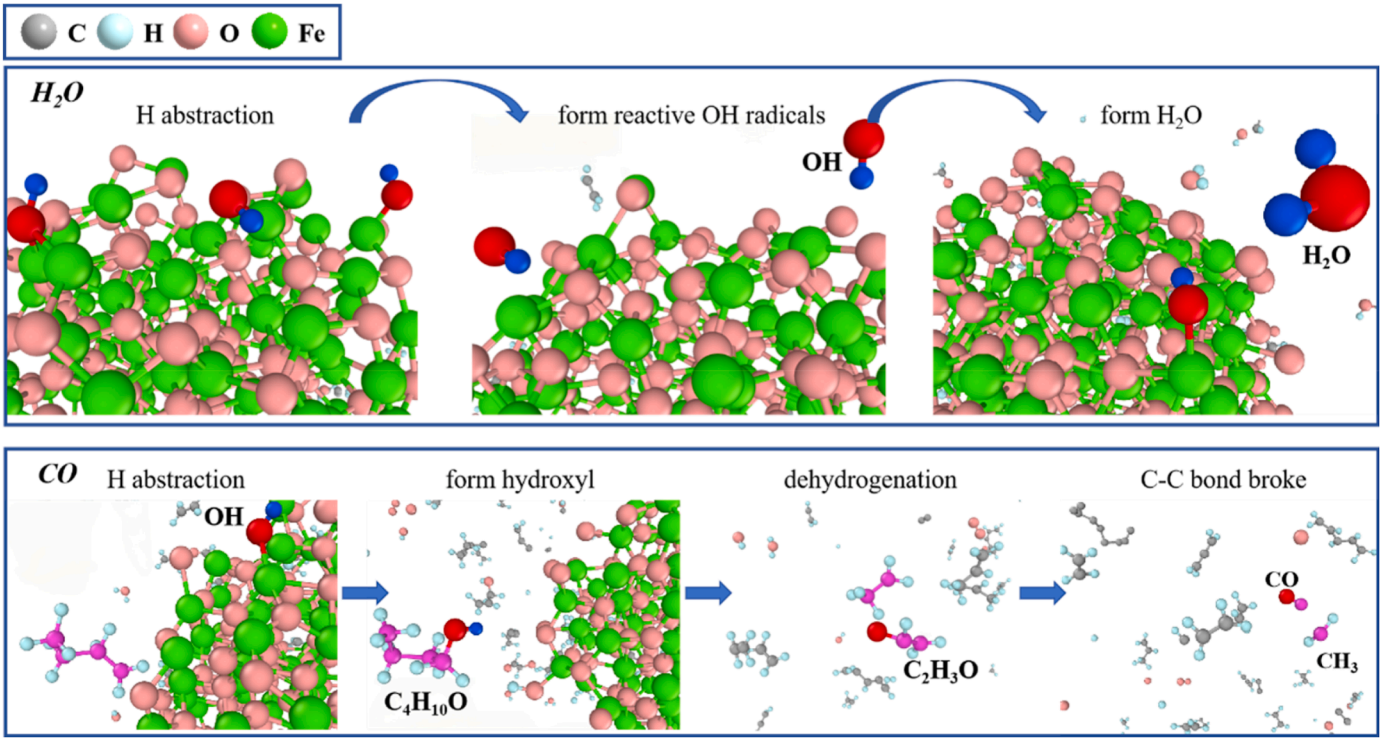


Fig. 9. Primary formation pathways of H_2O and CO in the CCP system. (Color scheme: gray - carbon, blue - hydrogen, pink - oxygen, green - iron).

analysis revealed significantly lower apparent activation energies for C-C (88.72 kJ/mol) and C-H (77.87 kJ/mol) bond scissions in the CCP system compared to the CP system (100.69 and 86.86 kJ/mol, respectively).

(3) Evolution analysis of Fe-O bonding and Fe-O coordination states indicated that lattice oxygen from Fe_2O_3 participated in the formation of oxidation products such as CO and H_2O. Higher pyrolysis temperatures promoted lattice-oxygen loss and increased the fraction of low-coordinated, oxygen-deficient Fe sites, suggesting the formation of oxygen-vacancy-like local defects during CCP system.

(4) Marked differences were observed in formation pathways of major gaseous products (CH_4, C_2H_2, C_2H_4, and CH_2O) between the two systems. The Fe_2O_3 catalyst not only modified CE depolymerization routes but also regulated the evolution of oxygen-containing functional groups. Moreover, surface oxygen atoms from Fe_2O_3 abstracted hydrogen from CE/PE to generate reactive OH radicals, ultimately enhancing H_2O and CO production.

The present results should be interpreted as relative mechanistic trends obtained under identical simulation conditions within the ReaxFF-MD simulate, rather than as direct predictions of experimental product yields or reactor-scale residence-time behavior. Although compared with published Py-GC/MS results provides qualitative external consistency for the predicted catalytic trends, but it does not constitute direct validation of the specific CE-PE-Fe_2O_3 atomistic mechanism. Future studies combining ReaxFF-MD with targeted experiments are needed to further verify the proposed oxygen-transfer and product-formation pathways. Furthermore, comprehensive studies on pyrolysis mechanisms of hemicellulose and lignin the other two major biomass components - are recommended to better reflect realistic biomass pyrolysis behavior.

CRediT authorship contribution statement

Sijia Li: Writing – review & editing, Writing – original draft, Visualization, Software, Investigation, Data curation. **Heping Li:** Writing – review & editing, Validation, Supervision, Project administration, Funding acquisition, Conceptualization. **Jianle He:** Investigation, Formal analysis. **Muye Feng:** Writing – review & editing, Methodology. **Zhengcheng Wen:** Validation. **Shenghao Wang:** Software. **Dingyi Wang:** Software. **Tianjun Shi:** Visualization. **Zhongze Bai:** Methodology. **Kaige Wang:** Funding acquisition.

Declaration of competing interest

The authors declare the following financial interests/personal relationships which may be considered as competing interests: Jianle He is employed by Huadian Electric Power Research Institute Co., Ltd. Other authors declare that they have no known competing financial interests or personal relationships that could have appeared to influence the work reported in this paper.

Acknowledgements

This work was supported by the National Key R&D Program of China (Grant No.2022YFE0135400) and National Natural Science Foundation of China (Grant No. 52236011).

Appendix A. Supplementary data

Supplementary data to this article can be found online at https://doi.org/10.1016/j.gerr.2026.100202.

References

Ahmed, M.H.M., et al., 2020. A review on advanced catalytic co-pyrolysis of biomass and hydrogen-rich feedstock: insights into synergistic effect, catalyst development and reaction mechanism. Bioresour. Technol. 310.
Aktulga, H.M., et al., 2012. Parallel reactive molecular dynamics: numerical methods and algorithmic techniques. Parallel Comput. 38 (4–5), 245–259.
Armenise, S., et al., 2021. Plastic waste recycling via pyrolysis: a bibliometric survey and literature review. J. Anal. Appl. Pyrolysis 158.
Bhoi, S., et al., 2014. Molecular dynamic simulation of spontaneous combustion and pyrolysis of brown coal using ReaxFF. Fuel 136, 326–333.
Bui, H.-H., et al., 2016. Pyrolysis of microalgae residues – a kinetic study. Bioresour. Technol. 199, 362–366.
Chen, C., et al., 2017. Reactive molecular dynamics simulations of biomass pyrolysis and combustion under various oxidative and humidity environments. Ind. Eng. Chem. Res. 56 (43), 12276–12288.
Chen, T., et al., 2021. High-temperature pyrolysis modeling of a thermally thick biomass particle based on an MD-derived tar cracking model. Chem. Eng. J. 417.
Feng, M., et al., 2021. A molecular dynamics study on oxidation of aluminum hydride (AlH3)/hydroxyl-terminated polybutadiene (HTPB) solid fuel. Proc. Combust. Inst. 38 (3), 4469–4476.
Feng, M., et al., 2024a. Atomistic insights into two-stage combustion of a single boron nanoparticle via reactive molecular dynamics. Fuel 375.
Feng, Y., et al., 2024b. Sintering mechanism of Fe_2O_3 particles during iron-based chemical looping combustion by using ReaxFF MD simulation and experiments. Energy Fuels 38 (10), 8928–8937.
Guda, V.K., Toghiani, H., 2016. Catalytic pyrolysis of pinewood using metal oxide catalysts in an integrated reactor system. Biofuels 8 (5), 527–536.
Gunasee, S.D., et al., 2017. Co-pyrolysis of LDPE and cellulose: synergies during devolatilization and condensation. J. Anal. Appl. Pyrolysis 126, 307–314.
Hu, B., et al., 2020. Recent progress in quantum chemistry modeling on the pyrolysis mechanisms of Lignocellulosic biomass. Energy Fuels 34 (9), 10384–10440.
Hu, B., et al., 2021. Pyrolytic characteristics and kinetics of Guanzhong wheat straw and its components for high-value products. Bioresources 16, 1958–1979.
Khatami, R., et al., 2012. Ignition characteristics of single coal particles from three different ranks in O_2/N_2 and O_2/CO_2 atmospheres. Combust. Flame 159 (12), 3554–3568.
Kimberly Chenoweth, A.C. T.v.D., Goddard, William A., 2008. ReaxFF reactive force field for molecular dynamics simulations of hydrocarbon oxidation. J. Phys. Chem. 1040–1053.
Krutof, A., Hawboldt, K.A., 2018. Upgrading of biomass sourced pyrolysis oil review: focus on co-pyrolysis and vapour upgrading during pyrolysis. Biomass Convers. Biorefinery 8 (3), 775–787.
Li, D., et al., 2021. Study on the pyrolysis behaviors of mixed waste plastics. Renew. Energy 173, 662–674.
Li, S., et al., 2023. Synergistic activity of the Fe_2O_3/Al_2O_3 catalyst for hydrogen production through pyrolysis-catalytic decomposition of plastics. ACS Sustain. Chem. Eng. 11 (27), 10108–10118.
Li, X., et al., 2021. ReaxFF molecular dynamics simulations of thermal reactivity of various fuels in pyrolysis and combustion. Energy Fuels 35 (15), 11707–11739.
Lin, X., et al., 2018. Catalytic fast pyrolysis of a wood-plastic composite with metal oxides as catalysts. Waste Manag. 79, 38–47.
Liu, J., et al., 2020. Biomass pyrolysis technology by catalytic fast pyrolysis, catalytic Co-Pyrolysis and microwave-assisted pyrolysis: a review. Catalysts 10 (7).
Liu, L., et al., 2025. Co-pyrolysis of biomass and plastic waste based on ReaxFF MD: insights into hydrogen migration, radicals interactions and synergistic mechanism. Energy 325.
Mao, Q., et al., 2017. Investigation of methane oxidation by palladium-based catalyst via ReaxFF Molecular Dynamics simulation. Proc. Combust. Inst. 36 (3), 4339–4346.
Mortensen, P.M., et al., 2011. A review of catalytic upgrading of bio-oil to engine fuels. Appl. Catal. Gen. 407 (1–2), 1–19.
Muhammad, I., Manos, G., 2021. Intensification of co-pyrolysis of plastic with biomass via pretreatment. Process Saf. Environ. Prot. 146, 586–598.
Mullen, C.A., et al., 2018. Catalytic co-pyrolysis of switchgrass and polyethylene over HZSM-5: catalyst deactivation and coke formation. J. Anal. Appl. Pyrolysis 129, 195–203.
Paajanen, A., Vaari, J., 2017. High-temperature decomposition of the cellulose molecule: a stochastic molecular dynamics study. Cellulose 24 (7), 2713–2725.
Pan, R., et al., 2022. Oil production from waste polyethylene and polystyrene co-pyrolysis: interactions of temperature and carrier gas flow rate. J. Environ. Chem. Eng. 10 (3).
Rahman, M.H., et al., 2021. Thermo-catalytic co-pyrolysis of biomass and high-density polyethylene for improving the yield and quality of pyrolysis liquid. Energy 225.
Rathnayake, D., et al., 2021. Investigation of biomass and agricultural plastic co-pyrolysis: effect on biochar yield and properties. J. Anal. Appl. Pyrolysis 155.
Russo, M.F., van Duin, A.C.T., 2011. Atomistic-scale simulations of chemical reactions: bridging from quantum chemistry to engineering. Nucl. Instrum. Methods Phys. Res. Sect. B Beam Interact. Mater. Atoms 269 (14), 1549–1554.
Shin, Y.K., et al., 2015. Development of a ReaxFF reactive force field for Fe/Cr/O/S and application to oxidation of butane over a pyrite-covered Cr_2O_3 catalyst. ACS Catal. 5 (12), 7226–7236.
Si, T., et al., 2019. ReaxFF study on the effect of CaO on cellulose pyrolysis. Energy Fuels 33 (11), 11067–11077.
Song, Q., et al., 2020. Pyrolysis of municipal solid waste with iron-based additives: a study on the kinetic, product distribution and catalytic mechanisms. J. Clean. Prod. 258.

Vanapalli, K.R., et al., 2021. Inhibitory and synergistic effects on thermal behaviour and char characteristics during the co-pyrolysis of biomass and single-use plastics. Energy 235.
Wachs, I.E., 2005. Recent conceptual advances in the catalysis science of mixed metal oxide catalytic materials. Catal. Today 100 (1–2), 79–94.
Wang, Y., et al., 2021. A study on co-pyrolysis mechanisms of biomass and polyethylene via ReaxFF molecular dynamic simulation and density functional theory. Process Saf. Environ. Prot. 150, 22–35.
Wang, Z., et al., 2021. Co-pyrolysis of waste plastic and solid biomass for synergistic production of biofuels and chemicals-A review. Prog. Energy Combust. Sci. 84.
Wei, X., et al., 2022. A ReaxFF molecular dynamic study on pyrolysis behavior and sulfur transfer during pyrolysis of vulcanized natural rubber. Waste Manag. 139, 39–49.
Wei, Z., et al., 2023. Mechanism investigations on co-pyrolysis of polyethylene and biomass using ReaxFF simulation and DFT computation. J. Environ. Chem. Eng. 11 (5).
Xie, S., et al., 2021. Prediction of pyrolyzate yields by response surface methodology: a case study of cellulose and polyethylene co-pyrolysis. Bioresour. Technol. 337.
Xie, W.-l., et al., 2023. Unraveling the radical chain mechanism in the pyrolysis of β-O-4 linked lignin: the role of aliphatic substituents. Proc. Combust. Inst. 39 (3), 3303–3311.
Xuan, W., et al., 2023. Exploration of the synergistic effect of co-pyrolysis of biomass and waste plastics based on ReaxFF-MD and DFT. J. Energy Inst. 111.
Yin, L., et al., 2024. Understanding hydropyrolysis mechanism of β-O-4 type lignin dimer. Chem. Eng. J. 488.
Yuan, H., et al., 2018. Study of synergistic effects during co-pyrolysis of cellulose and high-density polyethylene at various ratios. Energy Convers. Manag. 157, 517–526.
Yuan, X., et al., 2022. Carbon footprint and embodied carbon transfer at the provincial level of the Yellow River Basin. Sci. Total Environ. 803.
Zhan, W., et al., 2024. Effect of Fe and its oxides on steam gasification mechanism of lignin using ReaxFF molecular dynamics simulations. J. Energy Inst. 114.
Zhao, Y., et al., 2019. Synergistic effect of catalytic co-pyrolysis of cellulose and polyethylene over HZSM-5. J. Therm. Anal. Calorimetry 140 (1), 363–371.
Zheng, M., et al., 2016. Initial reaction mechanisms of cellulose pyrolysis revealed by ReaxFF molecular dynamics. Fuel 177, 130–141.
Zheng, M., Li, X., 2024. Co-pyrolysis behaviors of biomass and polymer plastics by using reactive molecular dynamics simulation. Energy 296.
Zou, C., et al., 2015. Molecular dynamics simulations of the effects of vacancies on nickel self-diffusion, oxygen diffusion and oxidation initiation in nickel, using the ReaxFF reactive force field. Acta Mater. 83, 102–112.